A Case Study Investigation into the Risk of Fatigue in Synchronous Flywheel Energy Stores and Ramifications for the Design of Inertia Replacement Systems

J. P. Rouse*[1], S. D. Garvey[1], B. Cárdenas[1], A. Hoskin[1], L. Swinfen-Styles[1] and W. Xu[2]

[1]*Department of Mechanical, Materials and Manufacturing Engineering, University of Nottingham, Nottingham, Nottinghamshire, NG7 2RD, UK*

[2]*Department of Mechanical and Electronic Engineering, Beihang University, Beijing, China*

Abstract

Flywheels are an attractive energy storage solution for many reasons; high turnaround efficiencies, long cycling lives and high "ramp-up" power rates have all been noted in the literature. Novel flywheel based hybrid energy storage systems have also been suggested by several authors which, due to the inherent partitioning of power sources in the system architecture, provide capacity for flywheels to deliver/receive energy over a comparatively large range of time scales and loading frequencies. Accommodating grid power fluctuations at the millisecond to second time scale is an ever growing problem that almost all grids undergoing de-carbonisation are facing. Synchronous flywheel energy storage systems have the attractive capability of being able to replace "real" (passively controlled) inertia with "real" inertia in a cheap and very robust manner. Flywheel design at the grid scale warrants careful consideration, as for static energy storage applications (i.e. those not used in transportation) the main driving factor is the reduction of manufacturing and material costs. It is paramount that material is used effectively, i.e. it is sufficiently stressed such that the flywheel is not oversized (and therefore expensive) while simultaneously guarding against the likelihood of catastrophic failure during service. Fatigue has the potential to be a serious life limiting mechanism due to fluctuating rotational speeds, however in depth analysis is lacking in the literature. The present work looks to quantify the severity of fatigue in flywheels which re-establish grid inertia by applying fatigue design methods (such as the rainflow cycle counting method and the generalised strain amplitude methods of Ince and Glinka for fatigue lifing) to loading scenarios that represent grid frequency fluctuations. Importantly flywheels are sized based on different limit stress criteria, thereby enabling differing levels of structural capacity usage between designs. For the realistic design cycles considered in the present work (representative of a large scale grid undergoing normal frequency fluctuations) all projected lives are extremely large, suggesting that fatigue is not a limiting factor and that any of the tested design methodologies is viable. Significant improvements in energy density and cost per unit of energy stored may however be achieved if elastic-perfectly-plastic (Tresca based) design criteria are implemented over simple strictly elastic variants. Neglecting containment costs for simplicity, improvements in energy density of $\approx 74\%$ and cost per unit of energy stored of $\approx 290\%$ are demonstrated to be achievable.

Keywords: *Fatigue, Flywheel, Inertia, Synchronous Machine.*

*Corresponding Author - James Rouse, Department of Mechanical, Materials and Manufacturing Engineering, University of Nottingham, Nottingham, Nottinghamshire, NG7 2RD, UK. Email: `James.Rouse@nottingham.ac.uk` Tel: +44 (0)115 84 67683

1 Nomenclature

A, B, C	Integration constants (flywheel stress equations)
b, c	Fatigue damage accumulation law coefficients
C_i	i^{th} kinematic hardening modulus
$\boldsymbol{\mathcal{C}}$	Fourth order elastic stiffness tensor
E	Young's modulus
E_K	Stored kinetic energy
f_{Grid}	Nominal grid frequency
f_{In}	Instantaneous grid frequency
Δf	Change in grid frequency
g	Yield function
H	Inertia time constant
J_2	Second invariant function
J_{FW}	Flywheel inertia
n_j	j^{th} cycle number
N_f	Number of cycles to failure
$\boldsymbol{\mathcal{N}}$	Unit vector normal to the yield surface
p	Number of machine poles
p_a	Accumulated equivalent plastic strain
P	Power to/from electric machine
P_R	"Real" inertia contribution to power
P_S	"Synthetic" inertia contribution to power
P_{SM}	Rated electric machine power
r	Radial position coordinate
R_i	Internal flywheel radius
R_o	External flywheel radius
$\boldsymbol{S}$	Deviatoric component of Cauchy stress tensor
t	Time
T	Resultant electric machine torque
u_z	Axial displacement
z	Axial coordinate
γ_i	$i^{th} kinematic dynamic recovery term$
$\Delta\gamma^e$	Elastic shear strain range
$\Delta\gamma^p$	Plastic shear strain range
$\boldsymbol{\epsilon}$	Total strain tensor
$\boldsymbol{\epsilon}_e$	Elastic strain tensor component
$\Delta\epsilon_n^e$	Elastic normal strain range
$\boldsymbol{\epsilon}_p$	Plastic strain tensor component
$\Delta\epsilon_n^p$	Plastic normal strain range
$\Delta\epsilon_{gen}^*$	Generalised strain range
ϵ_f'	Fatigue ductility limit
λ	Plastic multiplier
ν	Poisson's ratio
ρ	Density
$\boldsymbol{\sigma}$	Cauchy stress tensor
$\sigma_{n,max}$	Maximum normal stress component
σ_r	Radial stress component
σ_y	Initial yield stress
$\hat{\sigma}_Y$	Design limit stress
σ_f'	Fatigue strength
σ_θ	Hoop stress component
$\hat{\sigma}_\theta$	Maximum allowable hoop stress
τ_{max}	Maximum shear stress

τ_f'	Shear fatigue strength
χ	Back stress tensor
ω	Instantaneous rotational speed
ω_D	Design flywheel rotational speed
ω_{SM}	Synchronous machine speed
ω_{FW}	Instantaneous flywheel speed

2 Introduction

In any energy grid there is a constant need for balance between supply and demand. In future smart grids, which will no doubt increasingly draw on renewable sources, energy storage will play a vital role in ensuring an uninterrupted supply [1, 2]. Many time scales are involved in addressing this mismatch, from milliseconds to the order of weeks or months (diurnal and seasonal variations [3]), and all must be considered if stable grid is to be achieved [3]. Grid inertia limits the rate of change of frequency (RoCoF) when a sudden variation in load is encountered [4]. In thermal power plants, the physical inertia (i.e. that relating to a spinning mass) of a turbine passively controls the rate of change in speed to the synchronous machine it is coupled to. This action buys time for active control systems to take effect and stabilise the system frequency by adjusting prime mover inputs (note that this may not be required for a particular load imbalance scenario).

For a rotating mass, RoCoF may be defined as the rate of change of the rotor's rotational speed ω_{SM}. For a two pole electric machine equation (1) may be developed, wherein RoCoF ($d\omega_{SM}/dt$) is expressed in terms of machine torque required a change the rotor speed (T), the power required to change the rotor speed (P), and rotor inertia (J_{FW}). By considering the energy stored in a rotor and the power rating of the coupled electric machine (P_{SM}) a useful metric, H (the inertia time constant), is developed (see equation (2)). Study of H highlights important nuances relating to grid inertia. It is clear that the magnitude of an energy store cannot be considered in isolation to the power rating of the machine (or system) that couples the store to the grid. For inertia, both the scale of energy transactions (the magnitude of the energy store) and the rates at which these transactions can take place (the power rating of the machine linking the store to the grid) are important. Values of H between $2 - 10s$ are often reported in the literature [5] for thermal power plants. Assuming 2 pole 500 MW electric machines and a nominal UK generation frequency of 50 Hz, this would suggest total generation train (including machine rotors, exciters, and all turbine stages) inertias between $2x10^4$ and $1x10^5$ kgm^2. Similar inertia time constants are noted for wind turbines [6], however one must recall that renewable energy sources are commonly connected to the grid via power converters rather than synchronous generators and do not respond to system load directly (rather they operate at maximum available power). These power converters require control technology in order to keep line frequencies, voltages and power oscillations within acceptable tolerances while also guarding against power circulation [7]. It is debatable, therefore, as to whether or not this inertia is truly seen by the grid due to the interconnecting power electronics. What is clear is that "real" inertia (i.e. that resulting from spinning masses) has significant value in maintaining stable grids. As large thermal generation plants are retired and the grid is decarbonised, the resource of thermal power plant turbine inertia is diminished.

$$\frac{d\omega_{SM}}{dt} = \frac{T}{J_{FW}} = \frac{P}{J_{FW}\omega_{SM}} \tag{1}$$

$$H = \frac{\frac{1}{2}J_{FW}{\omega_{SM}}^2}{P_{SM}} \tag{2}$$

Inertia replacement systems are vitally important in renewable grids as they ensure stability can be maintained as loads and generators come on and off line. Flywheel energy storage systems are considered in the present work as these directly replace the "real" inertia of a turbine with the "real" inertia of a flywheel, thereby exploiting the benefits noted for thermal plants. The question now becomes how to appropriately design the flywheel (such that the best use of its load carrying capacity is made) given the cyclic nature of its operation and the potential for fatigue.

Flywheels have been a popular form of energy storage for hundreds of years. By citing the work of Schmidt *et al.* [8], a recent review by Pullen argued that the levelised cost of electricity for flywheel systems can compete with lithium ion battery technologies for primary frequency response (short duration, high frequency duty cycles) [9]. Central to this observation is that degradation is accounted for in the Monte-Carlo simulations performed by Schmidt *et al.* [8]. Pullen goes on to point out additional "costs" associated with popular lithium ion battery systems, highlighting the difficulties in securing key materials (raising ethical and sustainability concerns) and end of life treatment [9]. Interestingly, arguments have also been made in favour of flywheels in transport applications. Erdemir and Dincer, for example, recently considered electric bus flywheel systems [10]. By referencing both fuel economics and the nature of the duty cycles (that is to say, frequent acceleration and deceleration phases), Erdemir and Dincer argue hybrid flywheel energy stores are competitive with batteries and ultra-capacitors.

Flywheels are an attractive inertia replacement solution in de-carbonised grids as, when coupled with a synchronous machine, they can directly restore inertia in a high efficiency and environmentally friendly manner [2, 11, 12]. Some authors have however raised concerns that flywheels have relatively low energy density values [13]. Bouland suggests a value of 0.05 kWh/kg for metallic flywheels [14], whereas Pullen indicates 0.005 kWh/kg is representative if both rotor and casing (containment) requirements are considered. Some of this discrepancy can be accounted for by the fact Bouland considers only the rotating mass in the cost calculation, whereas Pullen includes both the rotor and casing (containment). Different limiting stresses are also used by the two authors, with the former opting for the ultimate tensile strength of a material and the latter opting for half the yield. This distinction in design limit stress and the effect it has on the characteristics of flywheel energy stores is central to the present work. Depending on duty cycle (i.e. the degree to which a flywheel is exercised and the hence the magnitude of stress amplitudes and the mean stress state) and the requirement for longevity, either of these limit stresses are defensible. Design limits based solely on monotonic mechanical behaviours are potentiality misleading however and may well lead to overly conservative designs. What is needed is a method to evaluate fatigue life that does presuppose elastic load conditions. The application of such a lifing method is the focus of the present work. It is clear that, in order to maximise energy density values, flywheels must be appropriately designed, either through material selection, geometry definition, or operating rotational speed [15]. As highlighted by Pullen [9], the energy storage capacity of a flywheel is proportional to the maximum allowable rotor stress. Choices of high density/high strength materials are limited (especially when unit material cost is considered as a design factor) and, in cases where a flywheel is "hard coupled" to a synchronous machine, operating speed is fixed by the machine architecture (number of poles) and supply/generation frequency. Flywheel geometry refinement is therefore an important area of research which warrants investment if flywheel returns are to be maximised [15, 14].

Many flywheel energy storage systems have been discussed in the literature, with numerous hybrid examples coupled to renewable energy sources such as photovoltaic cells [15, 2] and wind turbines [16, 17, 18]. For example, Hamzaoui *et al.* designed control systems for a flywheel energy store which provides slip energy to a 7.5 kW double fed induction generator (DFIG) wind turbine application, with supplementary pitch angle control used to achieve maximum power point tracking [19]. Flywheel control systems were also developed by Šonský and Tesař [20]. Specifically, electromagnetic bearing systems were progressed such that the energy extracted for stabilisation of five degrees of freedom was minimised. Of particular interest here are publications by Carrillo, Feijóo and Cidrás [21], where synchronous and asynchronous machines were attached to diesel generators and flywheel systems in order to compare their performance in supplementing wind power in isolated locations (i.e. for low power applications of approximately 50 kW). Building on the author's previous work, one synchronous machine/flywheel configuration featured a hydraulic transmission linking the two components. This was done in order to "allow energy transfer between two systems rotating at different speeds". During discharge, the flywheel would be spun down and used to drive a fixed displacement pump that circulates a pressurised fluid in line connected to a variable displacement motor. Work can thus be extracted by a motor to power a synchronous machine. Broadly speaking, variable speed configurations (asynchronous machines) were concluded to be superior for accommodating wind speed fluctuations and synchronous machines were better for demand load variations. The work of Barelli *et al.* showed that flywheel stores could improve battery life in residential micro-grids [22].

Numerous researchers have also looked to determine optimum flywheel geometries through some sort of optimisation procedure, however strucutral objective functions are typically simplistic in form. Arslan, for example, conducted a case study of plain and constant stress (tapered) flywheel geometries using elastic stress field solutions (with a simple limiting von Mises stress criterion determining ultimate dimensions), showing that energy density can be doubled with "smart" flywheel design [15]. Readers should note here that the work of Arslan assumes a disk type flywheel design; the potential for this type of benefit with more complex geometries (such as Laval or Stodola flywheels) is likely diminished and relatively poor volumetric energy densities will be realised. Jiang and Wu conducted 2D topology optimisation on high speed rotors by partitioning cross sections into three regions; an inner ring, an outer ring, and a centre region which may be modified by the optimisation procedure [23]. A distinction is often drawn between low speed and high speed flywheel energy storage systems [13], with the latter operating at speeds as high as $100,000$ rpm [2]. In Jiang and Wu's work, manufacture constraints, stress magnitudes, and volume fraction values were used to form objective functions with a penalised density method used to add/eliminate voxels. Rotors of approximately 800 mm in diameter, operating at 2250 rpm, were analysed, however only simple stress limits (200 MPa) were applied and no direct evaluation of fatigue life was made. Through the optimisation procedure improvements in energy densities of 14.3% were demonstrated. A similar study was reported by Pedrolli *et al.*, who looked to refine non-constant thickness flywheels using 2D axisymmetric finite element models and an evolution optimisation algorithm [24]. Flywheel cross sections were defined by 6 control points (the location of which could be modified by the optimisation algorithm) and a connecting spline. Optimisation objective functions were based on a maximum von Mises stress criterion (reference to a limit value) and the deviation of von Mises stress over the flywheel cross section. Results reproduced some well known features, such as the Stodola disk, and recommendations were made for further factors to be considered in the optimisation objective function. The present work effectively looks to establish a method which would allow fatigue to be introduced in such an optimisation. Flywheel structure was considered by Bouland *et al.* for transportation energy storage applications (200 kW permanent magnet machine systems) [14]. Fibrous materials with circumferential banding were suggested in order to reduce the number of pieces liberated in the case of a burst.

The structural analysis of flywheels has received some attention in the literature. Even so, the fundamental fatigue lifing approach utilised in the present work has not been applied to grid scale energy stores. Consequently, arguments on the proper design limit for large flywheel systems have been under-developed. Composite material flywheels have been a particular focus of structural analysis, having grown in popularity since the 1970s [9]. Tzeng and Moy considered the prevention of fatigue cracking in composite flywheel designs [25], suggesting (through the development of analytical expressions for stress fields in composite material flywheels) that axial reinforced and press fit shaft interfacing can significantly enhance the crack resistance properties of composite material flywheels. It should be noted however that, due to their comparatively high unit cost, composite materials are most suitable for flywheel design when rotational speeds are high. By way of example, the speeds considered by Tzeng and Moy are of the order of $50,000$ rpm. When rotational speed is set by the frequency of a grid, as is the case in a synchronous machine energy store system, steel is commonly considered to by the most appropriate choice [13]. It is worth noting here that there are at least three distinct driving motivations in flywheel energy store design (or, indeed, energy store design in general), namely designing for energy per unit volume, energy per unit mass, and energy per unit cost. Clearly the latter motivation is most relevant in large grid applications, however readers should remember the that choice of motivation (based on target application) determines which flywheel technology and design philosophy is most appropriate. The choice of composite material was studied by Conteh and Nsofor, who demonstrated that utilising a novel hybrid M46J/epoxy-T1000G/epoxy design over a more common place Boron/epoxy-Graphite/epoxy material combination could increase energy densities from 97.7 kJ/kg to 1718.54 kJ/kg [26]. An evaluation method for microcracking in carbon fibre flywheels was also developed in the work of Koch *et al.* and relied an the superposition of quasi static and fatigue simulation results [27]. Fatigue analysis of transport flywheel stores has been notably popular in the literature. Hearn *et al.* calculated the L10 life for bearing components in disc, arbour, and magnetically coupled planetary flywheel stores that could be used in fuel cell powered bus applications [28]. Hybrid vehicles were also the focus of Read *et al.*, wherein it was highlighted that flywheel system sizing and depth of discharge specification imposes structural requirements on the rest of the vehicle's transmission system [29]. Laminated flywheel stores for the light rail sector were considered by Shatil *et al.* through the simulation of local stress rising features (bolt holes, for example) in 3D finite element simulations [30]. The principles of linear elastic fracture mechanics were then applied, along with the well known Paris crack growth law, in order to estimate a maximum allowable crack size. Some inspiration for flywheel lifing methodologies may be drawn from studies performed on steam turbine rotors, however it is worth noting that the premature failure concerns in these applications typically focus on creep and fatigue interactions. High temperature damage mechanisms, such as those considered by the R5 procedure [31], are clearly of very limited interest to flywheel applications. Many turbine rotor lifing problems take a flaw tolerant approach, in which allowable defect sizes are calculated based on viscous (time dependent) material behaviours [32, 33].

Flywheels need to be designed such that the usage of structural material is maximised. Simple design criteria, such as elastic limit criteria, may be too conservative as many ductile materials can undergo a modest level of plasticity and harden with no significant detrimental effect on effective component life. Elastic-plastic criteria may be implemented, however the capacity for low cycle fatigue mechanism to limit life creates a certain level of concern. To date, most studies in flywheel design have neglected fatigue as a damaging mechanism. To the author's knowledge, the present work is the first time where candidate flywheel geometries, determined using simple design rules, are evaluated using general fatigue lifing methods and grid representative loading cycles. Large rotors are considered here for grid applications and, due to size, forming methods such as casting are not considered viable. Attention is therefore limited to multiple plate (or lamina) construction designs, meaning that plane stress assumptions are permissible. Hollow flywheels (those with an internal bore) are considered as this feature has value for shaft location purposes and additional energy supply (for example, through a compressed fluid supplying other components in hybrid storage systems). As discussed previously, synchronous machine applications are the focus of this work as flywheels have a potentially significantly role to play in inertia replacement strategies. Consequently, 2 and 4 pole machines are considered in order to maximise peripheral speed for finite diameters.

The present work utilises several analysis methods in the study of flywheel fatigue life. A brief overview is presented here in order to aid reader comprehension and the analysis process is shown diagrammatically in figure 1. The process begins with a definition of grid frequency history profile that indicates how the grid frequency fluctuates over the duty cycle. In the present work, these fluctuations have been determined through frequency analysis of grid disruption events (see section 3). For a given synchronous machine (here defined by a number of poles), the grid frequency fluctuations can be translated into a set of rotor speeds (see section 5), which may in turn be used to excite a non-linear finite element model such that multiaxial stress and strain (elastic and plastic) histories are developed. A kinematic hardening material model is implemented here for the description of elastic-plastic behaviours in 1045 steel (see section 4). Standard rainflow cycle counting algorithms are utilised to decompose the stress and strain histories into complete loading cycles. In doing this, mean and amplitude load values (stress and strain tensors) are calculated. These in turn can be used in generalised fatigue lifing methods (here based on the work of Ince and Glinka) to estimate failure life. Novelty in the present work is derived from the application of these distinct analysis methods to the problem of flywheel fatigue lifing. While each of the analysis methods is established in the literature, their combined application to laminar flywheels (which are popular design solutions for grid scale stores) is lacking from the literature. Indeed, detailed fatigue analysis of laminar flywheels of any sort is limited. Flywheel design methods are typically stress based and, in many cases, only elastic stress states are permitted. Common arguments against more ambitious design criterion centre around concerns over fatigue. The present work addresses a disconnect between appropriate flywheel design criteria (that allow for satisfactory utilisation of material structural capacity and enable improvements in energy storage characteristics) and concerns over the risk of premature fatigue failure.

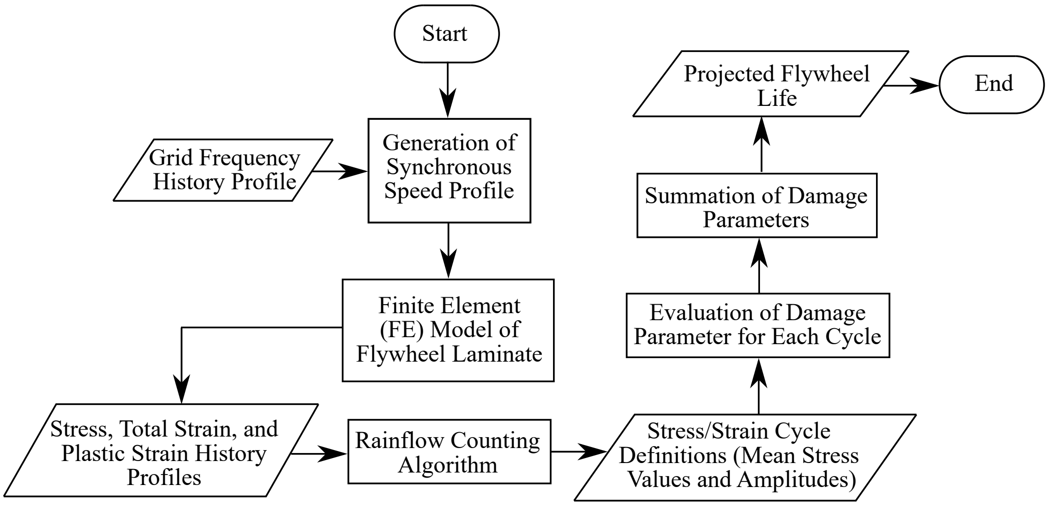

Figure 1: A flow chart illustrating the data flows and analysis methods used in the present work.

3 Grid Representative Frequency Fluctuations and Potential Flywheel Applications

Attention is limited here to the analysis of flywheel energy storage systems designed to re-introduce "real" inertia in large de-carbonised grids. The term real inertia is used here to identify systems in which power injection is controlled by the laws of motion only. An example of such a system would be the stiff coupling of a flywheel to a synchronous machine, similar to well known synchronous condenser designs (although such machines were not, originally, intended to provide inertia replacement). Synchronous condensers are, in a sense, very simple machines, as illustrated in figure 2 a). Here, a source a real inertia (a flywheel) is directly coupled to a synchronous electric machine. Mechanical energy can be extracted from the flywheel, at least temporarily, if the grid frequency drops and the synchronous machine rotor begins to de-accelerate. Clearly, the only way the flywheel can be recharged is through the synchronous machine, therefore such a system is not designed as an energy store as such. It is rather a balancing mechanism in which small positive and negative energy transactions are made, such that there is no nett transfer of energy. It is important to distinguish real sources of inertia from "synthetic" equivalents (for example, battery based systems), which require some overarching control system to determine the flow of power. Considering real inertia replacement applications places strict limitations on nominal operating speeds for the flywheel system.

The distinction between real and synthetic inertia is emphasised in the authors' previous work, wherein a "series hybrid kinetic energy store" (hereafter refereed to as SHyKESS) was developed [34] (see figure 2 b).). SHyKESS can be imagined as a flywheel store connected to a synchronous machine through a differential drive unit (DDU). The system is, in effect, a mechanical analogue of a doubly fed induction generator (DFIG), with the DDU allowing for the injection of slip energy. A difference between the synchronous machine rotor speed and the flywheel is therefore tolerated, meaning that SHyKESS can continue to act as a energy store even if the flywheel speed drops below what would normally be allowed by grid frequency limits. In this way, the flywheel can be exercised over a great range of operation and the usefulness of the energy capacity of the flywheel can be maximised. During the most common mode of operation the DDU is locked (it injects no slip energy into the system), meaning that the flywheel speed matches that of the machine rotor and SHyKESS behaves as a conventional synchronous flywheel energy store (i.e. all inertia can be considered to be real). A third type of inertia replacement system can, of course, be considered here, namely one in which all inertia is "synthetic" (i.e. does not emanate from rotating masses), as shown in figure 2 c). Some form of non-synchronous generation (high voltage direct current, HVDC, connections to wind turbines, for example) or energy store (battery banks, for example) can be used to balance the grid through the use of power electronics and sophisticated control systems. Clearly, such an application relies on robust control methods and power electronics are well known to be power limited, meaning the potential for overloading (during fault conditions, for example) is limited. Interested readers are directed to the author's previous work for a more comprehensive description of SHyKESS [34]. The relevance of these conditions will be made clear later in this section, as some loading profiles adopted in the present work exceed the bounds of what would normally be expected for a synchronous flywheel store. Note that, while references to flywheel axial lengths are omitted from the present work (the laminar flywheel design allows for modularity, after all), the authors' previous work sets out a case for square aspect ratios, wherein flywheel diameters and axial lengths are approximately equal [34]. The use of large flywheel rotors promotes the use of vacuum containment in order to minimise aerodynamic losses. It would make little sense in such a case to manufacture a thin vacuum chamber; the benefits of running in vacuum for a relatively low inertia system are outweighed by the cost of chamber manufacture. A good compromise can however be found for a square flywheel/chamber. For large rotor designs, standby losses can be further reduced through the adoption of magnetic bearing systems and vertically orientated rotors. In such a system, magnetic bearings provide much of the load carrying capability, while relatively small rotating element bearings ensure an acceptable dynamic stiffness. A case study application of SHyKESS which incorporates standing loss estimates may be found in the authors' previous work [34].

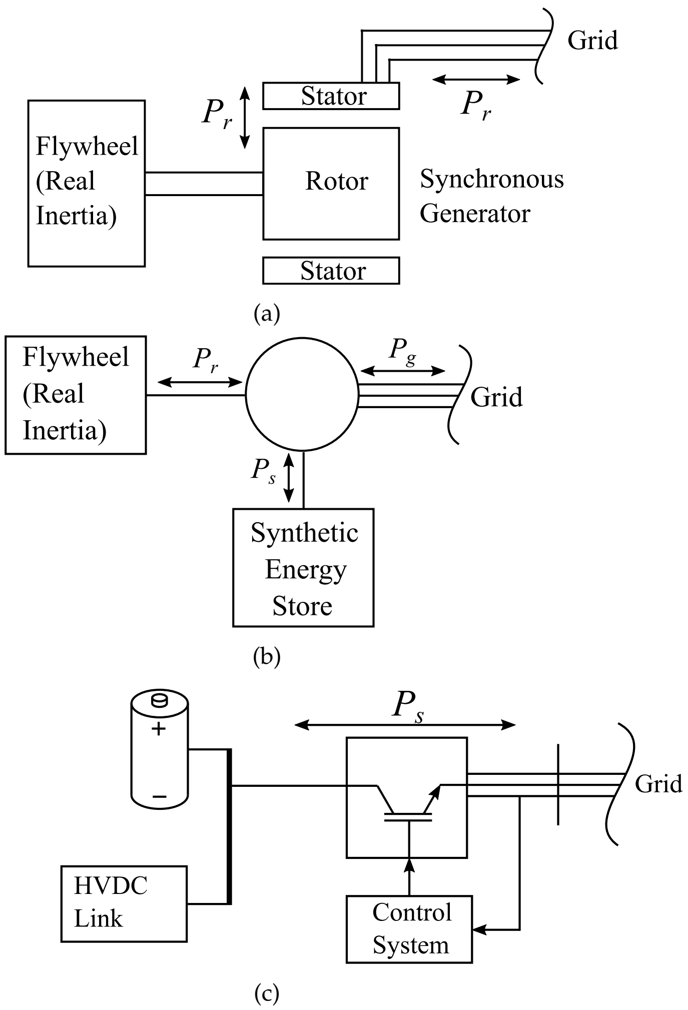

Figure 2: A potential classification of inertia sources, showing a). a completely real system (utilising only rotating inertia, as per a synchronous condenser), b). a hybrid system that mixes real and synthetic inertia sources (as per SHyKESS [34]), and c). a completely synthetic system. Note that P_r denotes power emanating from real inertia sources, whereas P_s denotes power emanating from synthetic energy sources.

Given the real inertia application, flywheel speed variations are governed by the RoCoF of the grid. In order to generate realistic and meaningful loading profiles several sets of data, generously provided by the UK's National Grid, have been analysed. Two distinct data sets are considered here; a 24 hour set (sampled at 1 Hz) in which large grid loads (pumps) are switched in and out, and a 2 second set (sampled at 50 Hz) which represents a 700 MW French inter-connector trip on the UK grid. These data sets represent nominal and fault grid conditions respectively, with the latter relating to an event which would likely require an enhanced frequency response. Note that in the latter case, frequency responses at "London" and "Manchester" locations were recorded, with the responses in figure 3 a). clearly showing the effects of a "non-rigid" grid (a rigid grid being one in which all points in the grid experience the same frequency at any instant). Example plots of all time series are presented in figure 3.

Time series data sets have been analysed using a discrete Fourier Transform (FFT) approach, thereby generating the spectra shown in figure 4. Simple sinusoidal grid frequency oscillations are not representative of real grid conditions, therefore a frequency analysis of grid frequency data is implemented here in order to determine the characteristics of grid frequency oscillations. The frequency characteristics of the grid frequency oscillations can be reassembled (using inverse Fourier transforms) to form periodic loading cycles that may be used to vary flywheel speeds and hence excite fatigue damage mechanisms. In order to generate test waveforms that can be readily discretised (over practical time steps) and implemented in non-linear analysis methods (see section 5), the spectrum relating to the 24 hour data has been partitioned about 0.01 Hz, thereby creating low and high frequency sub sets (see figure 4 a). and b)., respectively). The allows for loading cycles to be developed with time scales greater/less than periods of 1.66 minutes, thereby representing diurnal variations in f_{Grid} as well as the effects of sudden load disruptions, respectively. Note that the relationship between phase and amplitude is maintained for each discrete frequency component (that is to say, during inverse Fourier transforms, random phasing values are not applied to each grid frequency oscillation component). Loading waveforms, used to evaluate the risk of fatigue in various flywheel designs, are generated from these spectra. The most "damaging" components from the data sets are extracted, here summarised as the 5 highest amplitude components shown in figure 4. These have been used to create the representative loading cycles shown in figure 5. It is these cycles that will be used in fatigue analyses in the present work, where Δf represents a deviation from the nominal frequency of 50 Hz. Note that additional components where added in initial studies, however little influence was noted for values greater than 5. For convenience, the cycles are hereafter referred to as Cycle 24L, Cycle 24H, and Cycle IT, respectively. Cycle names have been chosen to indicate the source of the frequency components, namely the low frequency 24 hour data set spectrum, the high frequency 24 hour data set spectrum, and the inter-connector trip data set spectrum, respectively. An additional loading cycle is presented in figure 5 that has not been derived from the time series data in figure 3 (sub-figure d).), hereafter referred to as Cycle SHyKESS. Flywheel systems such as SHyKESS can accept large depth of discharge cycles. Cycle SHyKESS represents an arduous limit case for which fatigue failure should be a pressing concern. This is taken from the author's previous work [34].

The inclusion of a hybrid flywheel energy store in the present work allows for the consideration of greater depth of discharge cycles. This would, however, also decouple the flywheel rotational speed from the synchronous machine rotor speed (note that in synchronous condensers, these are always equivalent). The nature of control systems is outside the scope of the present work, there a simple relationship is assumed to relate instantaneous grid frequency (f_{In}) and instantaneous flywheel speed (ω_{FW}), see equation (3). It is assumed here that the flywheel rotor speed matches what would be the synchronous speed of the electric machine it is attached to at the instantaneous grid frequency f_{In}. The electric machine is characterised by the number of poles p. This assumption ensures that the DDU in the SHyKESS system can be locked near the nominal grid frequency while still allowing for decoupling in extended depth of discharge cycles.

$$\omega_{FW} = \frac{4\pi f_{In}}{p} \tag{3}$$

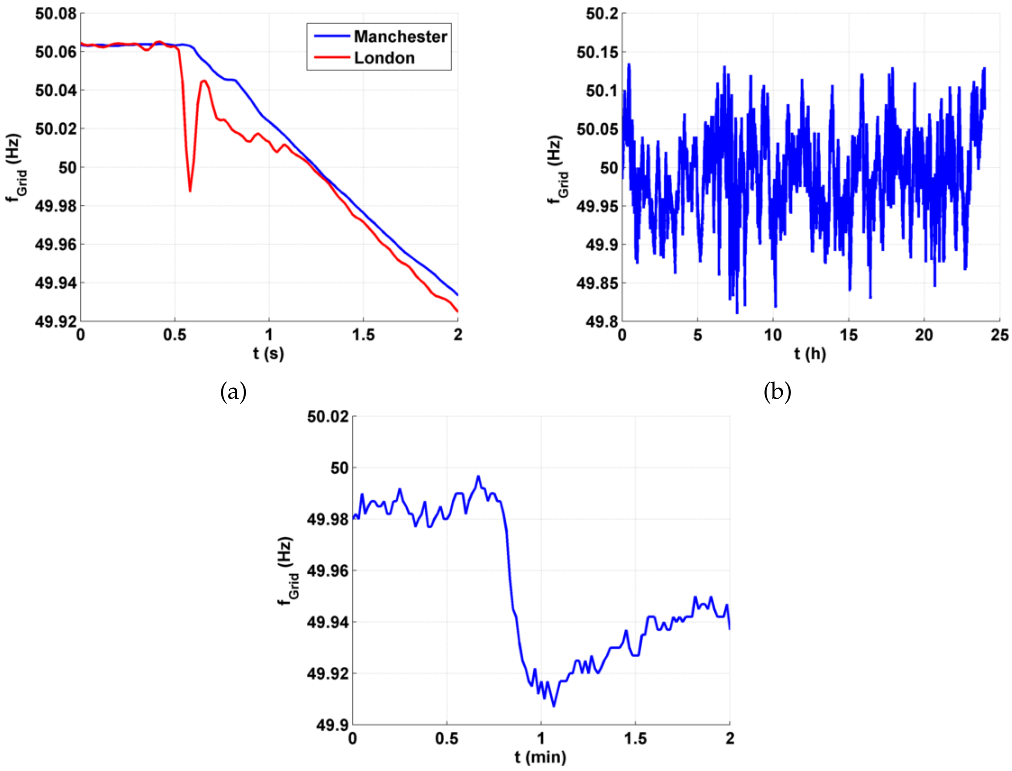

(a) (b) (c)

Figure 3: Time series of grid frequency (f_{Grid}) variations used in the present work, showing a). a 700 MW inter-connector trip event (2 second period), b). large grid loads coming in to and out of service (24 hour period), and c). a "close-up view" of a load coming in to service event (from the 24 hour period data set).

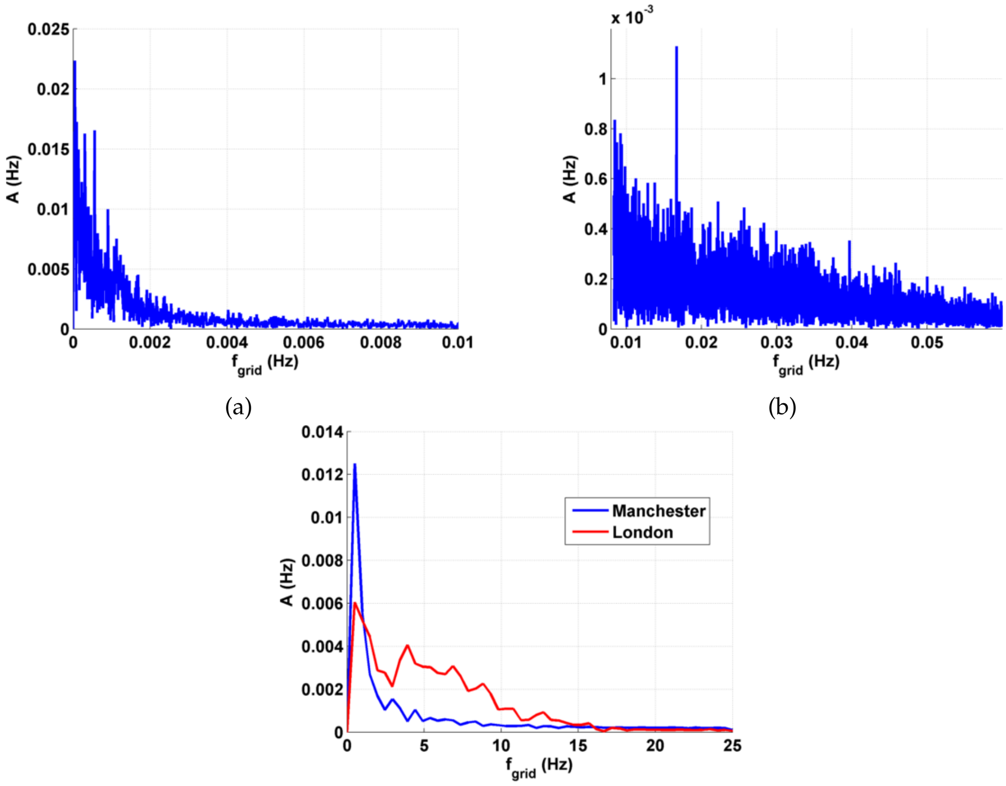

(a) (b) (c)

Figure 4: Amplitude spectrum plots (from FFT analysis of the data sets shown in figure 3), showing a). low frequency ($\leq 0.01\ Hz$) components in the 24 hour data set, b). high frequency ($\geq 0.01\ Hz$) components in the 24 hour data set, and c). components related to the inter-connector trip data set (measured at both London and Manchester).

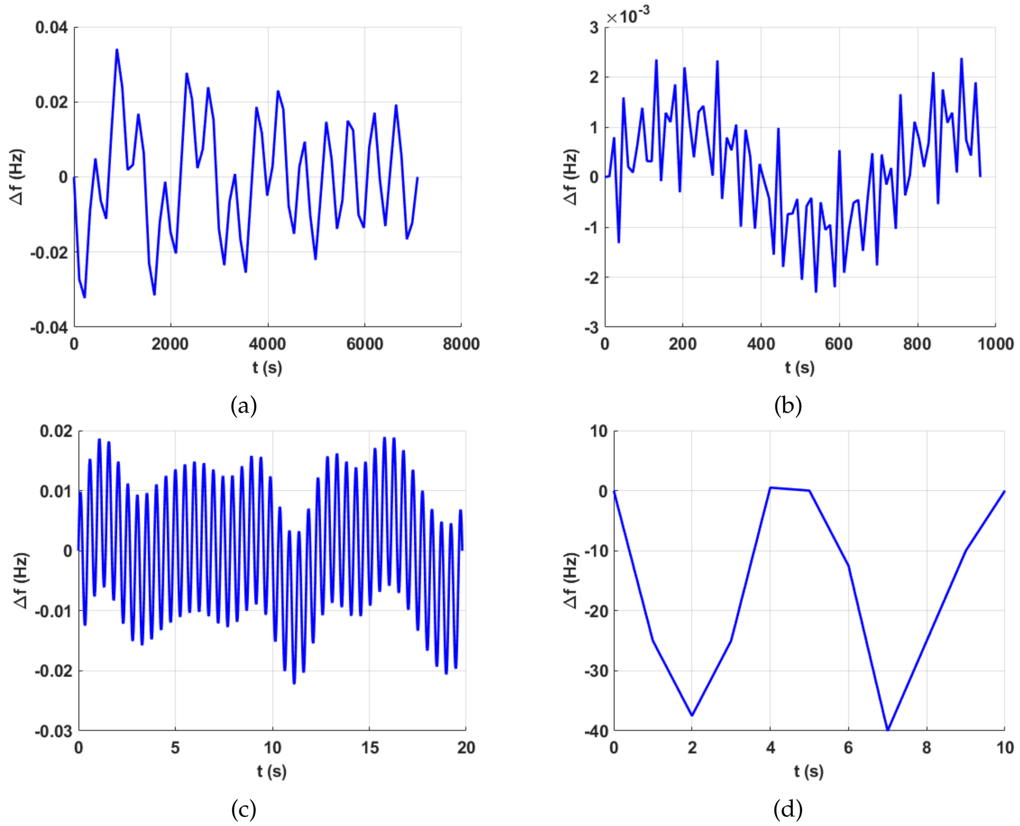

Figure 5: Loading cycles developed from the FFT analyses shown in figure 4, showing responses relating to a). low frequency 24 hour data set components (Cycle 24L), b). high frequency 24 hour data set components (Cycle 24H), c). inter-connector trip data set components (Cycle IT), and d). an arduous large depth of discharge cycle (Cycle SHyKESS).

4 Material Models and General Multi-axial Fatigue Lifing Models

The stress analysis work carried out here requires the definition of both a material model to describe the constitutive behaviour of the chosen flywheel material and a fatigue lifing model which, due to the wide range of potential loading conditions expected, must be generalised. The material assumed in the present work is an SAE 1045HRC medium carbon steel. High density and strength parameters are noted for this material and typical applications include ductility favouring components such as pressure vessels. Parameters used in simple material models (for the description of elastic and plastic deformation) are also widely available in the literature for 1045 steel, making the implementation of the material in the analysis straightforward [35]. It is worth noting that the 1045 steel assumed here is similar in terms of stiffness, ultimate tensile strength, density, and price to the 4340 steel referenced as a candidate flywheel material by Bouland *et al.* [14]. The 1045 steel tested by Whener and Fatemi was tempered at 176.67 ^{o}C for 1 hour, leading to a lower yield stress than that considered by Bouland and co-workers. In the present work this lower yield stress steel was chosen as, with the elastic-plastic design criterion outlined below, it results in flywheel geometries (specifically diameters) that are achievable in most steel foundries. Higher yield stress values would, with the design criterion discussed in section 5 , result in flywheel diameters that are larger than the capacity of most steel plate mills.

An elastic-plastic material model is required in order to describe material non-linearity in the FEA simulations performed in the present work. A simple elastic-plastic model is implemented here which assumes a von-Mises (J_2 invariant) yield function and the normality hypothesis. A two component Armstrong-Frederick back stress law is used to describe kinematic hardening (which is particularly relevant for the description of monotonic behaviour). Total strain, ϵ_T, is decomposed in to elastic, ϵ_e, and plastic, ϵ_p, components (see equation (4)). Elasticity is assumed to follow Hooke's law as shown in equation (5), where $\boldsymbol{\sigma}$ is the Cauchy stress tensor and $\boldsymbol{\mathcal{C}}$ is the fourth order elastic stiffness tensor (isotropic elasticity is assumed using Young's modulus E and Poisson's ratio ν).

$$\boldsymbol{\epsilon}_T = \boldsymbol{\epsilon}_e + \boldsymbol{\epsilon}_p \tag{4}$$

$$\boldsymbol{\sigma} = \boldsymbol{\mathcal{C}} : \left(\boldsymbol{\epsilon}_T - \boldsymbol{\epsilon}_p\right) \tag{5}$$

Plastic strain, $\boldsymbol{\epsilon}_p$, accumulates according to the normality hypothesis while obeying the consistency condition, as shown in equation (6). Note that rate terms are denoted by a dot above relevant quantities. When the yield function, g, is satisfied (i.e. $g = 0$), $\boldsymbol{\epsilon}_p$ accumulates in a direction normal to the yield surface (defined by the unit normal $\boldsymbol{\mathcal{N}}$) by a scalar amount defined by λ (the plastic multiplier). By substituting expressions for g, it may be shown that λ is equivalent to the accumulated plastic strain p_a (defined by equation (7)) and the deviatoric component of $\boldsymbol{\sigma}$, $\boldsymbol{S}$. A J_2 invariant based yield function is assumed, as shown in equation (8), where $\boldsymbol{\chi}$ is the total back stress and σ_y is the yield stress. A two component back stress decomposition is assumed, as shown in equation (9). Note that back stress decomposition allows for an improved representation of monotonic response, as discussed by Chaboche [36, 37, 38, 39]. The i^{th} back stress component evolves by an Armstrong-Frederick rule [40], where C_i is the i^{th} component hardening modulus and γ_i is a dynamic recovery exponent relating to the i^{th} back stress component ($\boldsymbol{\chi}_i$). The material model described here can be readily implemented in the commercial finite element solver ABAQUS using the in built combined hardening model.

$$\begin{aligned}\dot{\boldsymbol{\epsilon}}_p &= \dot{\lambda}\boldsymbol{\mathcal{N}} = \dot{\lambda}\frac{\partial g}{\partial \boldsymbol{\sigma}} \\ &= \frac{3}{2}\dot{p}_a \frac{\boldsymbol{S} - \boldsymbol{\chi}}{J_2\left(\boldsymbol{\sigma} - \boldsymbol{\chi}\right)}\end{aligned} \tag{6}$$

$$p_a = \left(\frac{2}{3}\boldsymbol{\epsilon}_p : \boldsymbol{\epsilon}_p\right)^{1/2} \tag{7}$$

$$g = J_2\left(\boldsymbol{\sigma} - \boldsymbol{\chi}\right) - \sigma_y \tag{8}$$

$$\boldsymbol{\chi} = \sum_{i=1}^{2} \boldsymbol{\chi}_i \tag{9}$$

$$\dot{\boldsymbol{\chi}}_i = C_i \dot{\boldsymbol{\epsilon}}_p + \boldsymbol{\chi}_i \gamma_i \dot{p}_a \tag{10}$$

Material parameter (E, σ_y, C_1, γ_1, C_2, and γ_2) values for the 1045 steel used in the present work have been determined using monotonic tensile data from Wehner and Fatemi [35]. For the sake of brevity the material parameter fitting procedure is omitted here. It should be noted, however, that the method is based on Cottrell's stress partitioning approach [41], uses a linear regression approach to determine the onset of plasticity, and may be found in the author's previous work [34, 42, 43]. The well known Ramberg-Osgood equation is used as a smoothing function in this procedure to limit the effect of noise in the experimental data. A summary of material parameters, used in both constitutive behaviour description and fatigue life estimation (to be described later) is presented in table 2. A density value of 7870 kg/m^3 is assumed for the 1045 material [44]. For reference, the uniaxial monotonic and cyclic material response predicted by the model is presented in figure 6 a). and b)., respectively. Note that, as would be expected, cyclic response stabilises after one cycle and the behaviour clearly displays the well known Bauschinger effect.

Table 2: Assumed material properties (monotonic, and cyclic) for SAE 1045HRC [35].

Parameter	Value
Young's Modulus, E	204 GPa
Poisson's Ratio, ν	0.30
Yield Strength, σ_Y	426 MPa
Ultimate Tensile Strength, σ_{UTS}	$----$
Hardening Modulus, C_1	$9.91x10^4$ MPa
Dynamic Recovery Coefficient, γ_1	$5.15x10^3$
Hardening Modulus, C_2	$2.72x10^5$ MPa
Dynamic Recovery Coefficient, γ_2	$7.65x10^2$
Fatigue Strength Coefficient, σ'_f	3372 MPa
Fatigue Strength Exponent, b	-0.1
Fatigue Ductility Coefficient, ϵ'_f	0.04
Fatigue Ductility Exponent, c	-0.4

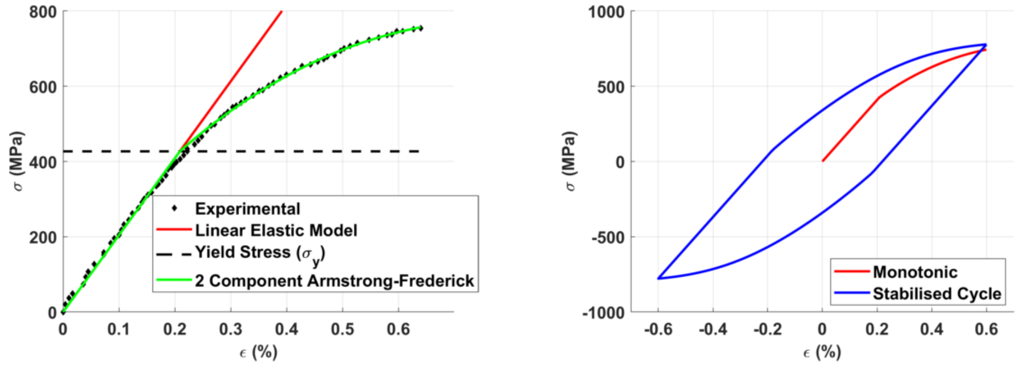

(a) (b)

Figure 6: The a). monotonic and b). cyclic uniaxial material response predicted for 1045 steel.

Fatigue life estimation over a large range of loading conditions is a difficult problem and there is no consensus in the community as to the best approach [45]. Fatigue lifing problems are commonly sub-divided into strain controlled low cycle fatigue and stress controlled high cycle fatigue analyses, with the former relating to the accumulation of plastic strain and failure lives less than 10,000 cycles and the latter usually related to an elastic structure response with associated failure live several orders of magnitude greater than those experienced in low cycle fatigue conditions. Due to the elastic-plastic response modelled in the present work, a generalised approach is required that can accommodate both these mechanisms. Many methods for mean stress correction (such as the well known Gerber, Goodman, and Soderberg methods) and fatigue life estimation (such as modified Smith-Watson-Topper [46], Manson-Coffin-Basquin [47], and Ramberg-Osgood relationships [48]) all experience difficulties when applied to general multi-axial loading conditions over such a wide range of structure responses.

The generalised strain approach of Ince and Glinka is adopted here due to its ability to collapse proportional and non-proportional loading fatigue life behaviours on to a single curve. Mean stress and path dependency corrections have also been demonstrated for 1045 steels [49]. A general strain amplitude ($\Delta\epsilon^*_{gen}/2$) may be calculated by equation (11), wherein an evaluation is made on all planes using the maximum shear stress (τ_{max}), the elastic and plastic shear strain amplitudes ($\Delta\gamma^e/2$ and $\Delta\gamma^p/2$, respectively), the maximum normal stress ($\sigma_{n,max}$), and the elastic and plastic normal strain amplitudes ($\Delta\epsilon^e_n/2$ and $\Delta\epsilon^p_n/2$, respectively). Scaling of stress quantities is achieved using the shear fatigue strength (τ'_f, given by equation (12) [50, 51]) and fatigue strength (σ'_f). Such an approach is generally termed a critical plane approach as a user must search for the most detrimental projection of the stress and strain tensors. Due to the dominance of hoop stresses and strains, the hoop direction is chosen as the normal for evaluation of equation (11) in the present work. Stress and strain tensors are then transformed by defining a rotation matrix about this axis, with the orientation that gives rise to peak generalised strain range values taken as the critical one. Discrete rotation angles are applied in order to limit computational effort here, with 2^o increments between evaluations. With the definition of an equivalent uniaxial strain range in hand, strain based relationships such as the one given in equation (13) may be used to approximate the number of cycle to fatigue failure N_f [46]. Fatigue strength (σ_f') and fatigue ductility limit (ϵ_f') parameters are used in conjunction with life exponents b and c to approximate high cyclic and low cycle life contributions, respectively. Standard rainflow cycle counting methods, such as those proposed by Matsuishi and Endo [52], are used to decompose the equivalent strain loading time series, with the damage attributed to a particular component calculated using the Palmgren-Miner rule [45] (see equation (14) for an example implementation with n cycle contributions).

$$\frac{\Delta\epsilon_{gen}^{*}}{2} = \left(\frac{\tau_{max}}{\tau_f'}\frac{\Delta\gamma^e}{2} + \frac{\Delta\gamma^p}{2} + \frac{\sigma_{n,max}}{\sigma_f'}\frac{\Delta\epsilon_n^e}{2} + \frac{\Delta\epsilon_n^p}{2}\right)_{max} = f(N_f) \tag{11}$$

$$\tau_f' = \frac{\sigma_f'}{\sqrt{3}} \tag{12}$$

$$f(N_f) = \frac{\sigma_f'}{E}\left(2N_f\right)^{2b} + \epsilon_f'\left(2N_f\right)^{c} \tag{13}$$

$$\sum_{j=1}^{n}\frac{n_j}{N_{f,j}} \leq 1 \tag{14}$$

5 Flywheel Stress Solutions and Design Conditions

One of several design methodologies may be applied in order to size a flywheel such that the value of its structural material is maximised. Cylindrical laminated (i.e. made from several stacked plates) flywheels are considered in the present work (these are sufficiently general as to be applicable for synchronous energy stores and can be readily scaled). As such, plane stress states are considered in the following calculations. The present section outlines three of these design strategies, all of which use simple stress based calculations in order to specify the out radius (R_o) of a flywheel for a given internal radius (R_i) and design speed (ω_D). Note that the present work considers synchronous machine applications only, meaning that ω_D is taken to be equivalent to the machine's synchronous speed ω_{SM} (given by equation (15), where p is the number of poles in the machine and f_{Grid} is the operating frequency, here taken to be a UK grid relevant 50 Hz). Readers are encouraged to note that plane stress states are assumed here as a convenient design tool (finite element models present later in this section do not make this restriction). Plane stress enforces a zero stress magnitude in the direction that is normal to the plane of loading which, in general, is not true to finite thickness plates. The conditions that need to be satisfied in order for the plane stress to be considered appropriate are therefore not well defined. A planar dimension to thickness ratio of 10:1 is sometimes quoted, however the suitability of this is very much situationally dependent. Note that radius to thickness ratios for flywheel used in the present work vary between 11.5 and 46.7 and very little through thickness stress variation is noted in the finite element models, suggesting that the plane stress assumption is appropriate here.

$$\omega_{SM} = \frac{4\pi f_{Grid}}{p} \tag{15}$$

Elastic solutions for the radial and hoop stresses (σ_r and σ_θ, respectively) in a rotating disk are widely known (see equations (16) and (17), where B and C are constants of integration and r is a radial position coordinate) and are used here in order to produce two conservative design conditions, namely that peak hoop stress ($\hat{\sigma}_\theta$, realised at $r = R_i$) is equal to half the yield stress ($\sigma_Y/2$, representing a design with a large factor of safety) and that $\hat{\sigma}_\theta = \sigma_Y$ (representing a flywheel designed to operate on the elastic limit). For hollow flywheels (i.e. where $R_i \neq 0$), R_o is found iteratively by assuming a trial value for R_o, enforcing boundary conditions (namely that $\sigma_R = 0$ at $r = R_i$ and $r = R_o$, note that no internal pressure is considered here as associated loads are generally small in comparison to centrifugal forces), solving for the stress distributions, and adjusting R_o to minimise the difference between the calculated $\hat{\sigma}_\theta$ and its limiting condition. Note that, when $R_i = 0$ (i.e. a solid flywheel), the integration constant C must equal 0 so that stresses remain finite. In this case, R_o may be determined by equation (18), where $\hat{\sigma}_Y$ is an effective yield stress for the given design condition (in the present work equal to $\sigma_Y/2$ or σ_Y).

$$\sigma_r = B - \frac{C}{r^2} - \frac{\rho\omega^2(3+\nu)}{8}r^2 \tag{16}$$

$$\sigma_\theta = B + \frac{C}{r^2} - \frac{\rho\omega^2(1+3\nu)}{8}r^2 \tag{17}$$

$$R_o = \sqrt{\frac{8\hat{\sigma}_Y}{\rho\omega^2\,(3+\nu)}} \tag{18}$$

A less conservative flywheel sizing procedure may be based on elastic-perfectly-plastic (EPP) material assumptions with a Tresca yield criterion (see Rees [53, 54]). Equation (19) describes equilibrium in a disk rotating at speed ω. The limiting case (burst) is considered to be when the material has yielded through the entire radius of the flywheel. The Tresca criterion and EPP material assumption therefore indicate that this occurs when $\sigma_\theta = \hat{\sigma_Y}$ for all r. Substituting this in equation (19) and integrating gives equation (20), where the constant A is determined using the boundary condition at $r = R_i$ (where $\sigma_r = 0$, see equation (21)). With this in hand, the external flywheel radius R_o may be found at a design speed (here taken to be $1.1\omega_D$, chosen such that a completely plastic flywheel is not realised at nominal operating speeds and the design retains some over-speed capacity) by enforcing the external boundary condition ($\sigma_r = 0$ at $r = R_o$). Fully plastic flywheel stress distributions (i.e. when $\omega = 1.1\omega_D$) can be seen in figure 7 (a). When $\omega \leq \omega_D$ stresses will transition from plastic (towards the centre of the flywheel) to elastic at some radial position R_{EP}. Solutions in these two regions are given by equation (20) and equations (16) and (17), respectively. R_{EP} may be found by enforcing continuity in σ_r over this boundary. Elastic/plastic stress distributions for $\omega = \omega_D$ are presented in figure 7 (b) (note R_{EP} is indicated by a dashed vertical line). As with the fully elastic design conditions, a convenient closed form solution for R_o may be developed for the elastic-perfectly-plastic case, given in equation (22).

$$\sigma_\theta - \sigma_r - r\frac{d\sigma_r}{dr} = \rho r^2\omega^2 \tag{19}$$

$$\sigma_r = \hat{\sigma_Y} - \frac{\rho r^2\omega^2}{3} + \frac{A}{r} \tag{20}$$

$$A = -R_i\left(\hat{\sigma_Y} - \frac{\rho {R_i}^2\omega^2}{3}\right) \tag{21}$$

$$R_o = \sqrt{\frac{3\hat{\sigma_Y}}{\rho\omega^2}} \tag{22}$$

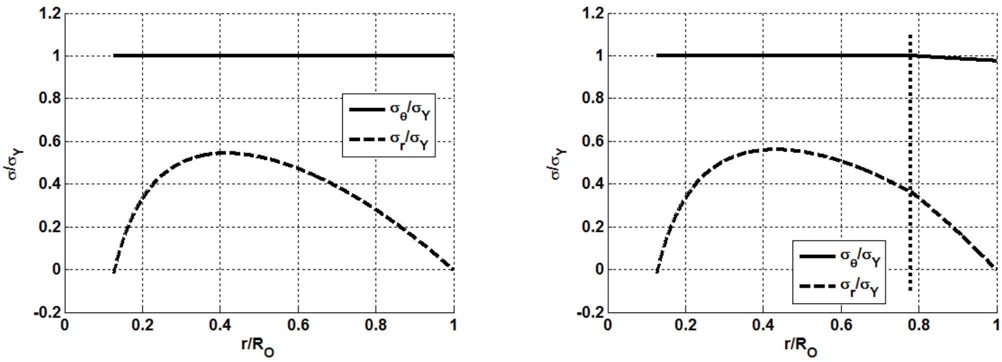

(a) (b)

Figure 7: Normalised flywheel stress distributions calculated using the Tresca elastic-perfectly-plastic solution for (a) the design speed case ($\omega = 1.1\omega_D$) and (b) the typical operating speed case (ω_D, 50 Hz equivalent).

Three simple design criteria have been described above which impose varying levels of conservatism on the design of a flywheel. A summary of flywheel geometries determined by these methods is given in table 3. Synchronous machine configurations with 2 and 4 poles are considered here as these will inevitably lead to the largest design speeds (see equation (15)). Solid ($R_i = 0$) and hollow flywheel designs are considered, with internal radii values chosen to represent a range relevant shaft diameters.

Table 3: Flywheel geometries (external radii) calculated using the three criterion assumed in the present work (namely $\hat{\sigma}_\theta = \sigma_Y/2$, $\hat{\sigma}_\theta = \sigma_Y$, and the elastic-perfectly plastic TRESCA condition) for 2 and 4 pole synchronous machine applications.

	2 Pole Machine $\omega_D = 100\pi \mathrm{rad}/s$			4 Pole Machine $\omega_D = 50\pi \mathrm{rad}/s$		
	$\hat{\sigma}_\theta = \frac{\sigma_Y}{2}$	$\hat{\sigma}_\theta = \sigma_Y$	TRESCA	$\hat{\sigma}_\theta = \frac{\sigma_Y}{2}$	$\hat{\sigma}_\theta = \sigma_Y$	TRESCA
$R_i = 0\ m$	0.816 m	1.154 m	1.167 m	1.633 m	2.309 m	2.335 m
$R_i = 0.1\ m$	0.575 m	0.815 m	1.114 m	1.153 m	1.632 m	2.283 m
$R_i = 0.2\ m$	0.570 m	0.811 m	1.054 m	1.151 m	1.630 m	2.228 m
$R_i = 0.4\ m$	0.547 m	0.795 m	0.915 m	1.140 m	1.622 m	2.109 m

A simple finite element analysis (FEA) model is used in the present work in order to solve for cyclic stress and strain fields in a flywheel made from the material described in section 4 (see figure 8). Axisymmetric quadratic reduced integration elements (CAX8R in ABAQUS/Standard) are used in order to reduce computational expense. Thin sections (0.05 m) are used in order to replicate plane stress conditions, with displacement in the axial direction (direction Z in figure 8) constrained on one plane and equation type constraint applied on the parallel face to ensure planar motion. Rotational forces are applied to the flywheel body by defining the rotational speed (based on the instantaneous values extracted from the design cycles in figure 5). Gravitational loads are neglected. A comparison of elastic stress profiles obtained by the FEA model and analytical solutions is shown in figure 9, displaying a good level of agreement between the two solutions methods.

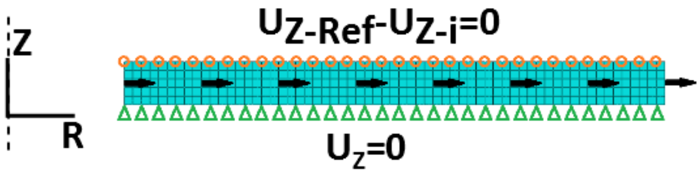

Figure 8: The axisymmetric FEA model used to analyse flywheel geometries subjected to fluctuating loads. Note that centrifugal loads are indicated by black arrows (these are body forces applied to the entirety of the model) and a planar constraint is applied to the top surface, such that the difference between any individual nodal displacement in z on this plane (u_{z-i}) and a reference node displacement in z (u_{z-Ref}) is 0.

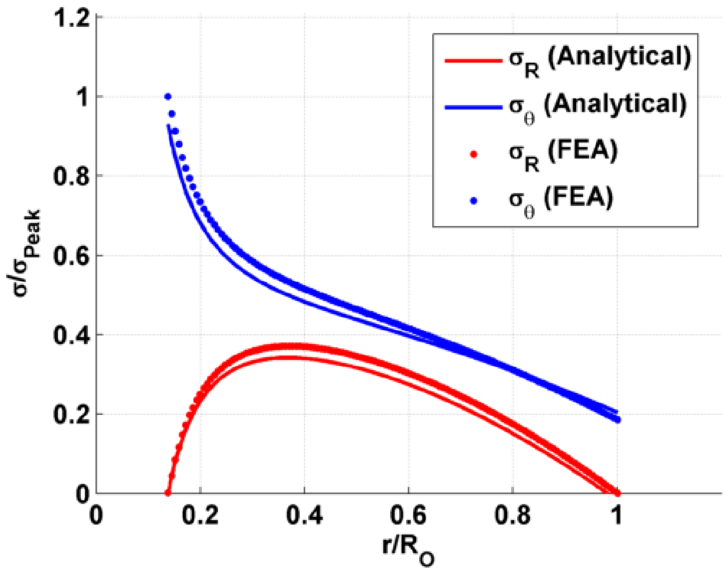

Figure 9: A comparison of elastic stress distributions calculated using analytical expressions (see equations (16) and (17)) and the FEA model shown in figure 8.

6 Results and Discussion

Fatigue life estimation results are presented in table 4 and table 5, with damage fractions ($D_{Fraction}$, evaluated using the Palmgren-Miner rule given in equation (14)) attributed to the design cycles Cycle 24L, Cycle 24H, Cycle IT, and Cycle SHyKESS along with projected failure lives t_f (expressed in years). Projected failure lives are calculated using the duration of the loading cycles (see figure 5) and observing the point at which the damage fraction achieves unity. This is clearly conservative as it assumes the flywheel is only subjected to one loading condition throughout its life and it does not account for the non-linear accumulation of damage. This simplistic method is implemented here in order to help visualise the comparative risk of adopting one of the three flywheel design methods. Of the loading cycles derived from grid event data (see figure 3) Cycle IT (relating to fault conditions and enhanced frequency response) is the most damaging cycle. This is to be expected of course, as the amplitudes and sub-cycle frequencies associated with Cycle IT are far greater (by two orders of magnitude) than those associated with loadings Cycle 24L and Cycle 24H. It should be noted however that projected failure lives (determined by taking cycle time and multiplying by the inverse of $D_{Fraction}$; a highly conservative lifing hypothesis) are relatively insensitive to flywheel design criterion (i.e. the maximum allowable stress). This suggests that damage fractions associated with each rainflow sub-cycle fall on the upper limit of the damage model. Differences between these three cycle failure lives are can be attributed to the different loading cycle durations (see figure 5) and the different number of rainflow sub-cycles. For all of the grid based loading cycles failure lives are extremely large, suggesting that fatigue is not a limiting design factor at present. The outer diameters reported in table 3 are, at a maximum 4.67 m. This is approaches the capacity of most of the world's steel mills (for example, JFE steel in Japan can, at a maximum, produce plates 5 m in width [55]), indicating that manufacture constraints are likely to limit flywheel dimensions before fatigue failure. Flywheels in the present work are designed using simple limit stress based design criterion. As such, under elastic dominate loading conditions, similar stress and strain states will be induced in each flywheel design. Loading cycles Cycle 24L, Cycle 24H, and Cycle IT bring about small variations in rotational speed which, given the over-speed design mentioned in section 5, give rise to such elastic states. The stress/strain based lifing criterion implemented in the present work therefore predicts identical fatigue lives for all geometries when excited by Cycle 24L, Cycle 24H, and Cycle IT loading cycles, leading to the omission of geometry data in table 4. Note that the same is not true for Cycle SHyKESS, wherein large grid frequency fluctuations (see figure 5) result in different levels of plasticity in each flywheel designed and thus differences in projected fatigue life.

Cycle SHyKESS is, of course, the most damaging of all loading cycles. In grid data based loading cycles frequency fluctuations are small (peak component amplitudes are 0.022 Hz). Many hybrid systems have been proposed which allow for extended discharge/charge of the flywheel (through the use of a continuously variable transmission, or CVT, for example), meaning that rotational speed variations have the potential to be significant. Cycle SHyKESS attempts to represent such a variation. Failure lives calculated for Cycle SHyKESS are highlighted in table 5. The difference between flywheel design criterion becomes evident for the arduous Cycle SHyKESS loading conditions. For solid flywheels, there exists a two orders of magnitude difference between fatigue lives calculated for conservative flywheel designs ($\hat{\sigma}_\theta = \sigma_Y/2$) and those that allow for the onset of plasticity ($\hat{\sigma}_\theta = \sigma_Y$ and TRESCA variants). When hollow flywheels are considered a two orders of magnitude difference is maintained between fatigue lives calculated for $\hat{\sigma}_\theta = \sigma_Y/2$ and $\hat{\sigma}_\theta = \sigma_Y$ design methodologies. Hollow flywheels designed using the TRESCA methodology are over 10,000 times smaller than the $\hat{\sigma}_\theta = \sigma_Y/2$ equivalent. These general trends are consistent for all internal bore diameters and each electric machine variant.

The kinetic energy (E_K) stored in a flywheel may be given by equation (23), where J_{FW} is the moment of inertia (see equation (24), where m is flywheel mass). Using these expressions evaluations of energy density (kWh/kg), volumetric energy density (kWh/m^3), and cost per unit of energy stored ($\$/kWh$) may be made for the geometries given by the three design rules used here (geometries are summarise in table 3). Flywheel energy characteristics are summarised in table 6. Note that, in the case of volumetric energy density calculations for hollow flywheels, the volume "saving" due to the central hole is neglected (i.e. flywheel volume is calculated using R_O only). The volumetric energy density metric provides information on how well energy stores can be packaged. In the case of hollow flywheels, the central hole presumably carries a transmission shaft (albeit a potentially hollow one), meaning that this volume cannot be utilised for any useful purpose and should not be considered as a benefit when calculating volumetric energy density. It is also crucial to note that, in the present work, containment costs or volume requirements are not incorporated into indicative calculations. A unit cost of \$0.89/kg is assumed here for the 1045 steel raw material[56]. Although processing/manufacturing is not explicitly costed in the present work, the indicative costs in table 6 highlight the inexpensive nature of flywheel systems and provide a useful metric to compare design solutions. As discussed above, fatigue lifing is not, in most cases, a contributing factor to design for the loading cycles considered in the present work. Designs which allow for some level of plasticity are therefore potentially viable. In addition to the energy characteristic measures summarised in table 6, potential "savings" are presented in table 7. Savings are here calculated by taking the TRESCA design characteristic as a reference, calculating the difference to one of the elastic design condition ($\hat{\sigma}_\theta = \sigma_Y/2$ or $\hat{\sigma}_\theta = \sigma_Y$) characteristics, and normalising with respect to the corresponding TRESCA characteristic. Note that like flywheels are compared with like (for example, 2 pole machine solid TRESCA flywheel characteristics are compared with 2 pole machine solid $\hat{\sigma}_\theta = \sigma_Y$ flywheel characteristics). The results presented in table 7 therefore indicate the loss in energy density and increase in cost incurred if conservative design methods (e.g. $\hat{\sigma}_\theta = \sigma_Y/2$ or $\hat{\sigma}_\theta = \sigma_Y$) are implemented over ones which better utilise material strength (e.g. TRESCA).

Careful design of the flywheel can increase energy density and volumetric energy density values by 74.35% (by, for example, designing a flywheel using a TRESCA criterion rather than a $\hat{\sigma}_\theta = \sigma_Y/2$ criterion). Cost per unit of energy stored may also be improved by over 200% if TRESCA criterion designs are implemented over $\hat{\sigma}_\theta = \sigma_Y/2$ variations, for hollow flywheels. This is due to the stress concentration effect of including an internal bore in a flywheel. In elastic designs this severely limits outer radius, however the yielding offered by elastic-perfectly-plastic designs reduces this. Significant improvements are not realised in solid flywheels (savings of around 2% are observed for all metrics) due to the lack of a stress concentration and the rapid increase in plasticity as outer diameter is increased. That is to say, for solid flywheels, the adoption of a TRESCA design methodology does not result in a significantly bigger flywheel than a $\hat{\sigma}_\theta = \sigma_Y$ design methodology, as yielding by the TRESCA yield criterion occurs at nearly the same flywheel diameter where $\hat{\sigma}_\theta = \sigma_Y$. Note that this is not true in flywheels with a hole, where there is a significant difference between the flywheel diameter that causes $\hat{\sigma}_\theta = \sigma_Y$ and the flywheel diameter that satisfies the TRESCA yield criterion. It is interesting to compare the solid flywheel characteristics developed here to commercial monolithic flywheel storage systems, such as those produce by Amber Kinetic [57] and Temporal Power [58]. By approximating rotor masses of $\approx 4000kg$ and stored energy capacities of $30 - 50kWh$ for both systems, energy densities between 6×10^{-3} and 9×10^{-3} kWh/kg may be crudely estimated for these systems (based on published rotor masses, dimensions, and operating speeds [57, 58]). Referring to table 6, it can be seen that these values fall between the $\hat{\sigma}_\theta = \sigma_Y/2$ and plastic design criterion energy densities suggested in the present work. This observation suggests that elastic design criterion were used to develop the Amber Kinetic and Temporal Power systems and that the improvements discussed here for laminar flywheels may be applicable to monolithic designs.

$$E_K = \frac{1}{2} J_{FW} \omega^2 \tag{23}$$

$$J_{FW} = \frac{1}{2} m (R_o^2 + R_i^2) \tag{24}$$

Table 7: A summary of energy density (kWh/kg, equivalent to volumetric energy density, kWh/m^3), and cost per unit of energy stored ($\$/kWh$) savings (%), comparing $\hat{\sigma}_\theta = \frac{\sigma_Y}{2}$ and $\hat{\sigma}_\theta = \sigma_Y$ solutions to TRESCA criterion equivalents.

		2 Pole Machine $\omega_D = 100\ \pi\text{rad}/s$		4 Pole Machine $\omega_D = 50\ \pi\text{rad}/s$	
Reference		$\hat{\sigma}_\theta = \frac{\sigma_Y}{2}$	$\hat{\sigma}_\theta = \sigma_Y$	$\hat{\sigma}_\theta = \frac{\sigma_Y}{2}$	$\hat{\sigma}_\theta = \sigma_Y$
$R_i = 0m$	kWh/kg	51.11	2.22	51.09	2.21
	$\$/kWh$	-104.53	-2.27	-104.46	-2.26
$R_i = 0.1m$	kWh/kg	72.77	46.1	74.35	48.81
	$\$/kWh$	-267.26	-85.55	-289.88	-95.33
$R_i = 0.2m$	kWh/kg	68.29	39.38	72.73	46.1
	$\$/kWh$	-215.41	-64.95	-266.65	-85.55
$R_i = 0.4m$	kWh/kg	53.95	20.58	68.32	39.43
	$\$/kWh$	-117.16	-25.91	-215.69	-65.1

7 Conclusions

The effective design of flywheels requires that material is appropriately loaded such that its structural value is maximised. The present work has analysed frequency fluctuations in the UK grid and applied derived design cycles to candidate flywheel geometries (assuming plane stress/thin lamina construction) using a general fatigue lifing procedure of Ince and Glinka. The aim of this work is not to predict accurate fatigue failure lives of flywheels. The low damage fractions associated with most of the rainflow sub-cycles results in the implementation of a limit damage value. The simulations conducted here compare flywheel designs using a common fatigue life metric. A significant difference in projected fatigue lives is only noted for "arduous" loading cycles that would not normally be realised in simple flywheel energy stores. Whether the risk associated with a particular design methodology can be accepted depends on a number of factors, which include the provision for containment and the expected

Table 4: Damage fractions ($D_{Fraction}$) and projected failure lives (t_f, given in years) calculated for the design cycles Cycle 24L, Cycle 24H, and Cycle IT (evaluated for the geometries derived in table 3). Note that no variation in projected fatigue lives is noted between different flywheel geometries due to near identical stress states being induced in each model.

		2 Pole Machine $\omega_D = 100\ \pi\text{rad}/s$			4 Pole Machine $\omega_D = 50\ \pi\text{rad}/s$		
		$\hat{\sigma}_\theta = \frac{\sigma_Y}{2}$	$\hat{\sigma}_\theta = \sigma_Y$	TRESCA	$\hat{\sigma}_\theta = \frac{\sigma_Y}{2}$	$\hat{\sigma}_\theta = \sigma_Y$	TRESCA
Cycle 24L	$D_{Fraction}$	3.20×10^{-14}	3.20×10^{-14}	3.20×10^{-14}	3.20×10^{-14}	3.20×10^{-14}	3.20×10^{-14}
	t_f (yrs)	$7.02 \times 10^{+09}$	$7.02 \times 10^{+09}$	$7.02 \times 10^{+09}$	$7.02 \times 10^{+09}$	$7.02 \times 10^{+09}$	$7.02 \times 10^{+09}$
Cycle 24H	$D_{Fraction}$	4.00×10^{-14}	4.00×10^{-14}	4.00×10^{-14}	4.00×10^{-14}	4.00×10^{-14}	4.00×10^{-14}
	t_f (yrs)	$7.61 \times 10^{+08}$	$7.61 \times 10^{+08}$	$7.61 \times 10^{+08}$	$7.61 \times 10^{+08}$	$7.61 \times 10^{+08}$	$7.61 \times 10^{+08}$
Cycle IT	$D_{Fraction}$	1.24×10^{-13}	1.24×10^{-13}	1.24×10^{-13}	1.24×10^{-13}	1.23×10^{-13}	1.24×10^{-13}
	t_f (yrs)	$5.06 \times 10^{+06}$	$5.06 \times 10^{+06}$	$5.06 \times 10^{+06}$	$5.06 \times 10^{+06}$	$5.08 \times 10^{+06}$	$5.06 \times 10^{+06}$

Table 5: Damage fractions ($D_{Fraction}$) and projected failure lives (t_f, given in years) calculated for the design cycle Cycle SHyKESS (evaluated for the geometries derived in table 3).

		2 Pole Machine $\omega_D = 100\ \pi\text{rad}/s$			4 Pole Machine $\omega_D = 50\ \pi\text{rad}/s$		
		$\hat{\sigma}_\theta = \frac{\sigma_Y}{2}$	$\hat{\sigma}_\theta = \sigma_Y$	TRESCA	$\hat{\sigma}_\theta = \frac{\sigma_Y}{2}$	$\hat{\sigma}_\theta = \sigma_Y$	TRESCA
$R_i = 0\ m$	$D_{Fraction}$	3.28×10^{-09}	1.52×10^{-06}	1.83×10^{-06}	3.34×10^{-09}	1.53×10^{-06}	1.85×10^{-06}
	t_f (yrs)	$9.66 \times 10^{+01}$	2.09×10^{-01}	1.73×10^{-01}	$9.51 \times 10^{+01}$	2.07×10^{-01}	1.72×10^{-01}
$R_i = 0.1\ m$	$D_{Fraction}$	3.62×10^{-09}	1.68×10^{-06}	7.96×10^{-05}	3.64×10^{-09}	1.69×10^{-06}	1.03×10^{-04}
	t_f (yrs)	$8.77 \times 10^{+01}$	1.89×10^{-01}	3.98×10^{-03}	$8.71 \times 10^{+01}$	1.88×10^{-01}	3.08×10^{-03}
$R_i = 0.2\ m$	$D_{Fraction}$	3.68×10^{-09}	1.70×10^{-06}	4.40×10^{-05}	3.76×10^{-09}	1.71×10^{-06}	7.98×10^{-05}
	t_f (yrs)	$8.62 \times 10^{+01}$	1.87×10^{-01}	7.20×10^{-03}	$8.43 \times 10^{+01}$	1.85×10^{-01}	3.97×10^{-03}
$R_i = 0.4\ m$	$D_{Fraction}$	3.34×10^{-09}	1.62×10^{-06}	9.52×10^{-06}	3.70×10^{-09}	1.71×10^{-06}	4.47×10^{-05}
	t_f (yrs)	$9.51 \times 10^{+01}$	1.95×10^{-01}	3.33×10^{-02}	$8.57 \times 10^{+01}$	1.86×10^{-01}	7.10×10^{-03}

Table 6: Energy density (kWh/kg), volumetric energy density (kWh/m^3), and cost per unit of energy stored ($\$/kWh$) evaluations for the flywheel geometries given in table 3.

		2 Pole Machine $\omega_D = 100\ \pi\text{rad}/s$			4 Pole Machine $\omega_D = 50\ \pi\text{rad}/s$		
		$\hat{\sigma}_\theta = \frac{\sigma_Y}{2}$	$\hat{\sigma}_\theta = \sigma_Y$	TRESCA	$\hat{\sigma}_\theta = \frac{\sigma_Y}{2}$	$\hat{\sigma}_\theta = \sigma_Y$	TRESCA
$R_i = 0m$	kWh/kg	4.56×10^{-03}	9.13×10^{-03}	9.33×10^{-03}	4.57×10^{-03}	9.14×10^{-03}	9.34×10^{-03}
	kWh/m^3	35.9	71.8	73.4	35.9	71.9	73.5
	$\$/kWh$	195.	97.5	95.3	194.	97.4	95.2
$R_i = 0.1m$	kWh/kg	2.33×10^{-03}	4.62×10^{-03}	8.57×10^{-03}	2.30×10^{-03}	4.58×10^{-03}	8.95×10^{-03}
	kWh/m^3	17.8	35.8	66.9	17.9	35.9	70.2
	$\$/kWh$	381.	192.	103.	387.	194.	99.4
$R_i = 0.2m$	kWh/kg	2.50×10^{-03}	4.78×10^{-03}	7.89×10^{-03}	2.34×10^{-03}	4.62×10^{-03}	8.57×10^{-03}
	kWh/m^3	17.2	35.3	59.8	17.8	35.8	66.9
	$\$/kWh$	355.	186.	112.	380.	192.	103.
$R_i = 0.4m$	kWh/kg	3.15×10^{-03}	5.43×10^{-03}	6.83×10^{-03}	2.50×10^{-03}	4.78×10^{-03}	7.90×10^{-03}
	kWh/m^3	11.5	31.9	43.5	17.2	35.3	59.9
	$\$/kWh$	282.	163.	130.	355.	186.	112.

likelihood of various loading scenarios being encountered. This works illustrates however that there exists a great potential to re-consider the limits of structural design in energy stores. If less conservative limits can be tolerated significant benefits, both in terms of energy density and capacity cost, can be realised.

Failure in the present work can be interpreted as the initiation of a crack in an initially crack free component. The determination of a critical initial crack length (given cyclic loading) may serve as a more useful and selective structural design criterion. This should be investigated in future work using a "comparison of design methodologies" approach implemented in the present work. Flywheel designs that plastically deform the structural material will, ideally, harden and achieve elastic shakedown after some period of transition. If a material isotropically softens and the flywheel design accumulates a sufficient amount of plastic strain during initial loading this may not be possible. Future work should therefore also look to implement more sophisticated material models to quantify this risk. It should be noted also that the fatigue lives calculated here are based on a simple addition of damage fractions. Frequency domain based fatigue life estimations are difficult due to the strong influence of mean loading, however approximate methods have been developed (the Durlik equations for example, recently reviewed in the work of Quigley *et al.* [59]) which could be implemented in detailed future studies. Loading cycles implemented in the present work have, for the most part, assumed current grid characteristics and frequency fluctuations. A question therefore inevitably presents itself - how representative of future decarbonised grids are these fluctuations? Perhaps counter-intuitively, the more inertia replacement systems utilised on grid the less they are exercised, as the grid has (potentially) enough reserve to accommodate imbalances without large frequency deviations and RoCoFs. The characteristics of decarbonised grids and the associated risk of fatigue in flywheels is therefore difficult to predict as is hinges upon how serious the problem of grid inertia is judged by operators and regulators. It is assumed in the present work that a consistent level of inertia is maintained through decarbonisation, however this assumption itself raises an interesting future research question. The relationship between generation "nodes" and large loads will likely change in future grids. In the UK, for example, offshore wind will likely be brought onshore from the North Sea at either the west cost of Scotland or along the coast of East Anglia. This is dramatically different to historic power generation provisions. Given the dynamics of the grid (frequency fluctuations are not "seen" at all points in the grid simultaneously), there is an interesting open question on how inertia replacement systems can enable this shift by accounting for potentially large frequency deviations in geographical regions which, historically, relied on local generation inertia.

8 Acknowledgements

The presented work is funded by the EPSRC (EP/R001251/1) and incorporates collaborations with the Energy Technologies Institute (ETI), Power Continuity Systems and Quartzelec Ltd. The authors would also like to express their sincere thanks to National Grid for their open exchange of grid data.

References

[1] Sørensen, B . Energy intermittency. CRC Press; 2014.

[2] Mousavi G SM, Faraji F, Majazi A, Al-Haddad K. A comprehensive review of flywheel energy storage system technology. Renewable and Sustainable Energy Reviews. 2017;67:477–490.

[3] Jain P. Wind energy engineering. McGraw Hill; 2010.

[4] Díaz-González F, Sumper A, Gomis-Bellmunt O. Energy storage in power systems. Wiley; 2016.

[5] Thiesen H, Jauch C. Determining the load inertia contribution from different power consumer groups. Energies. 2020;13:1588.

[6] Bassi F, Caciolli L, Giannuzzi G, Corsi N, Giorgi A. Use of hidden inertia from wind generation for frequency support in power grids. In: AEIT International Annual Conference (AEIT), 2016; 2016. .

[7] Keyhani A, Marwali MN, Dai M. Integration of green and renewable energy in electric power systems. Wiley; 2010.

[8] Schmidt O, Melchior S, Hawkes A, Staffell I. Projecting the future levelized cost of electricity storage technologies. Joule. 2019;3:81–100.

[9] Pullen KR. The status and future of flywheel energy storage. Joule. 2019;3:1394–1399.

[10] Erdemir D, Dincer I. Assessment of renewable energy-driven and flywheel integrated fast-charging station for electric buses: A case study. Journal of Energy Storage. 2020;30:101576.

[11] Soomro A, Amiryar ME, Pullen KR, Nankoo D. Comparison of performance and controlling schemes of synchronous and induction machines used in flywheel energy storage systems. Energy Procedia. 2018;151:100–110.

[12] Mansour M, Mansouri MN, Bendoukha S, Mimouni MF. A grid-connected variable-speed wind generator driving a fuzzy-controlled PMSG and associated to a flywheel energy storage system. Electric Power Systems Research. 2020;180:106137.

[13] Arani AAK, Karami H, Gharehpetian GB, Hejazi MSA. Review of flywheel energy storage systems structures and applications in power systems and microgrids. Renewable and Sustainable Energy Reviews. 2017;69:9–18.

[14] Bouland B, Bernhoff H, Leijon M. Flywheel energy and power storage systems. Renewable & sustainable energy reviews. 2007;11:235–258.

[15] Arslan MA. Flywheel geometry design for improved energy storage using finite element analysis. Materials and Design. 2008;29:514–518.

[16] Prodromidis GN, Coutelieris FA. Experimental and theoretical investigation of flywheel-based energy storage in off-grid power plants using renewables. Journal of Energy Engineering. 2016;142:04014055–1–8.

[17] Prodromidis GN, Coutelieris FA. Simulations of economical and technical feasibility of battery and flywheel hybrid energy storage systems in autonomous projects. Renewable Energy. 2012;39:149–153.

[18] Sebastián R, Peña Alzola R. Control and simulation of a flywheel energy storage for a wind diesel power system. Electrical Power and Energy Systems. 2015;64:1049–1056.

[19] Hamzaoui I, Bouchafaa F, Talha A. Advanced control for wind energy conversion systems with flywheel storage dedicated to improving the quality of energy. International Journal of Hydrogen Energy. 2016;41:20832–20846.

[20] Šonský J, Tesař V. Design of a stabilised flywheel unit for efficient energy storage. Journal of Energy Storage. 2019;24:100765.

[21] Carrillo C, Feijóo A, Cidrás J. Comparative study of flywheel systems in an isolated wind plant. Renewable Energy. 2009;34:890–898.

[22] Barelli L, Bidini G, Bonucci F, Castellini L, Fratini A, Gallorini F, et al. Flywheel hybridization to improve battery life in energy storage systems coupled to RES plants. Energy. 2019;173:937–950.

[23] Jiang L, Wu CW. Topology optimization of energy storage flywheel. Structural and Multidisciplinary Optimization. 2017;55:1917–1925.

[24] Pedrolli L, Zanfei A, Ancellotti S, Fontanari V, Benedetti M. Shape optimization of a metallic flywheel using an evolutive system method: Design of an asymmetrical shape for mechanical interface. Proceedings of the Institution of Mechanical Engineers, Part C: Journal of Mechanical Engineering Science. 2018;232:217–230.

[25] Tzeng JT, Moy P. Composite energy storage flywheel design for fatigue crack resistance. In: 14th Symposium on Electromagnetic Launch Technology; 2008. .

[26] Conteh MA, Nsofor EC. Composite flywheel material design for high-speed energy storage. Journal of Applied Research and Technology. 2016;14:184–190.

[27] Koch I, Just G, Otremba F, Berner M, Gude M. Analysis of the micro-cracking behaviour of carbon fibre reinforced flywheel rotors considering residual stresses. Composite Structures. 2018;204:587–593.

[28] Hearn CS, Flynn MM, Lewis MC, Thompson RC, Murphy BT, Longoria RG. Low cost flywheel energy storage for a fuel cell powered transit bus. In: IEEE Vehicle Power and Propulsion Conference; 2007. .

[29] Read MG, Smith RA, Pullen KR. Optimisation of flywheel energy storage systems with geared transmission for hybrid vehicles. Mechanism and Machine Theory. 2015;87:191–209.

[30] Shatil G, Ren XJ, Wang L. Assessment of fatigue and fracture strength of transportation energy storage flywheel using finite element simulation. In: Conference: Damage and Fracture Mechanics VII; 2002. .

[31] Ainsworth RA, Hooton DG. R6 and R5 procedures: The way forward. International Journal of Pressure Vessels and Piping. 2008;85(3):175–182.

[32] Dong-mei J, Jia-qi S, Quan S, Heng-Chao G, Jian-xing R, Quan-jun Z. Optimization of start-up scheduling and life assessment for a steam turbine. Energy. 2018;160:19–32.

[33] Zhu X, Chen H, Xuan F, Chen X. On the creep fatigue and creep rupture behaviours of 9-12turbine rotor. European Journal of Mechanics - A/Solids. 2019;76:263–278.

[34] Rouse JP, Garvey SD, Cárdenas B, Davenne TR. A series hybrid "real inertia" energy storage system. Journal of Energy Storage. 2018;20:1–15.

[35] Wehner T, Fatemi A. Effects of mean stress fatigue behaviour on hardened carbon steel. International Journal of Fatigue. 1991;13:241–248.

[36] Chaboche JL. A review of some plasticity and viscoplasticity constitutive theories. International Journal of Plasticity. 2008;24:1642–1693.

[37] Chaboche JL. Time-independent constitutive theories for cyclic plasticity. International Journal of Plasticity. 1986;2:149–188.

[38] Chaboche JL, Rousselier G. On the plastic and viscoplastic constitutive-equations - part 1: Rules developed with internal variable concept. Journal of Pressure Vessel Technology - Transactions of the ASME. 1983;105:153–158.

[39] Chaboche JL, Rousselier G. On the plastic and viscoplastic constitutive-equations - part 2: Application of internal variable concepts to the 316 stainless-steel. Journal of Pressure Vessel Technology - Transactions of the ASME. 1983;105:159–164.

[40] Frederick CO, Armstrong PJ. A mathematical representation of the multiaxial Bauschinger effect. Materials at High Temperatures. 2007;24(1):1–26.

[41] Cottrell AH. Dislocations and plastic flow in crystals. Oxford University, London. 1953.

[42] Kyaw ST, Rouse JP, Lu J, Sun W. Determination of material parameters for a unified viscoplasticity-damage model for a P91 power plant steel. International Journal of Mechanical Sciences. 2016;115-116:168–179.

[43] Rouse JP, Hyde CJ, Sun W, Hyde TH. Comparison of several optimisation strategies for the determination of material constants in the Chaboche visco-plasticity model. Journal of Strain Analysis for Engineering Design. 2013;48:347–363.

[44] ;. Available from: `http://www.matweb.com/search/datasheet_print.aspx?matguid=193434cf42e343fab880e1dabdb143ba`.

[45] Collins JA, Busby H, Staab G. Mechanical design of machine elements and machines: A failure prevention perspective. John Wiley & Sons; 2010.

[46] Ince A, Glinka G. A modification of Morrow and Smith-Watson-Topper mean stress correction models. Fatigue & Fracture of Engineering Materials & Structures. 2011;34:854–867.

[47] Wang Y, Susmel L. The modified Manson-Coffin curve method to estimate fatigue lifetime under complex constant and variable amplitude multiaxial fatigue loading. International Journal of Fatigue. 2016;83:135–149.

[48] Nieslony A, el Dsoki C, Kaufmann H, Krug P. New method for evaluation of the Manson-Coffin-Basquin and Ramberg-Osgood equations with respect to compatibility. International Journal of Fatigue. 2008;30:1967–1977.

[49] Ince A, Glinka G. A generalised fatigue damage parameter for multiaxial fatigue life prediction under proportional and non-proportional loadings. International Journal of Fatigue. 2014;62:34–41.

[50] Yu ZY, Shu SP, Liu Q, Liu Y. Multiaxial fatigue damage parameter and life prediction without any additional material constants. Materials. 2017;10:1–15.

[51] McClaflin D, Fatemi A. Torsional deformation and fatigue of hardened steel including mean stress and stress gradient effects. International Journal of Fatigue. 2004;26:773–784.

[52] Marsh G, Wignall C, Thies PR, Barltrop N, Incecik A, Venugopal V, et al. Review and application of Rainflow residue processing techniques for accurate fatigue damage estimation. International Journal of Fatigue. 2016;82:757–765.

[53] Rees DWA. The mechanics of solids and structures. Imperial College Press; 2016.

[54] Rees DWA. Elastic-plastic stresses in rotating discs by von Mises and Tresca. Journal of Applied Mathematics and Mechanics. 1999;79:281–288.

[55] ;. Available from: http://www.jfe-steel.co.jp/en/products/plate/catalog/c1e-001.pdf.

[56] ;. Available from: http://www.tritonalloysinc.com/en-10025-2-steel/steel-plate-bs-en-10025-2-steel-grade-plate/steel-plate-type-c-45-plate/.

[57] Amber Kinetics; 2020. Available from: https://www.amberkinetics.com/wp-content/uploads/2020/05/Amber-Kinetics-DataSheet.pdf.

[58] Temporal Power; 2017. Available from: https://www.ieso.ca/en/Powering-Tomorrow/Technology/High-Performance-Flywheel-Energy-Storage-Systems-Temporal-Power.

[59] Quigley J, Lee Y, Wang L. Review and assessment of frequency-based fatigue damage models. SAE International Journal of Materials and Manufacturing. 2016;9:565–577.